ADVANCES IN MATERIALS SCIENCE, Vol. 26, No. 3 (89), September 2026

DOI: 10.2478/adms-2026-0010

Mostafa M. Basheir[1*], Ruchi Nair[1], Mukesh P. Chaudhari[1], Biplob Sen[1], Meki K. Bedasa[1], Rania Hasan[2] and Hitesh D. Patel[1]

[1] *Department of Chemistry, Gujarat University, Navrangpura, Ahmedabad-380009, Gujarat, India*
[2] *Department of Mechanical Engineering, Marwadi University, Rajkot-360003, Gujarat, India*

[*] *mostafageo6@gmail.com*

COMPOSITION-DRIVEN INDIRECT STRUCTURAL DEFECT ENGINEERING IN NEAR-EUTECTIC Sn-Zn AND Sn-Cu-Zn-Sb-Pb ALLOYS: STRUCTURAL COMPLEXITY AND ELECTRICAL FUNCTIONALITY

ABSTRACT

This study contrasts a near-eutectic Sn-Zn alloy (Sn-1) with a multicomponent Sn-Cu-Zn-Sb-Pb system (Sn-2) to elucidate the interplay between compositional complexity, phase formation, and electrical transport. While conventional characterization confirms expected phase evolution, the results reveal a decisive trade-off: Sn-1 achieves superior conductivity (1.105×10^5 S/cm), whereas Sn-2 exhibits a marked reduction (26.7%). This degradation is not merely compositional but structurally driven, as increased chemical complexity promotes intermetallic formation that intensifies electron scattering. The findings challenge the simplistic assumption that multicomponent design inherently enhances performance, highlighting instead that excessive complexity can be detrimental to electrical efficiency.

Keywords: *Sn-based alloys; defect engineering; electrical conductivity*

INTRODUCTION

The ideal crystal structure represents a purely theoretical state, as real materials inevitably deviate from such perfect periodic arrangements. These deviations are commonly referred to as structural defects [1]. Such defects may arise at different dimensional scales within the crystal lattice, ranging from point defects at the atomic scale to extended defects that involve larger regions of the structure, including volumetric defects. Despite their different forms, these defects constitute a critical factor in generating lattice distortions and altering the electronic nature of materials, which in turn influences a wide range of functional properties, including electrical, optical, and catalytic properties [2–4]. Within this context, the concept of defect engineering has emerged as an effective strategy for the design of advanced materials. This approach relies on the deliberate control of the type, density, and distribution of defects within the host matrix in order to enhance the physical, chemical, and functional performance of materials [5–9]. For instance, the introduction of foreign atoms into the crystal lattice of a host element (doping) can generate new electronic states that modify the surface behavior of

Received: 15.05.2026; Received in revised form: 01.07.2026; Accepted: 27.07.2026

catalytic materials. In addition, defects may be introduced through mechanical processes such as rolling, forging, and drawing, or through physical methods such as irradiation. Collectively, these approaches represent direct mechanisms for structural defect engineering [10, 11]. Conversely, the concept of indirect defect engineering can be established as a strategic approach for defect management through the precise tuning of elemental composition, achieved by the intentional control of the type, number, and proportion of constituent elements within a material. In such systems, compositional complexity, together with variations in atomic size and electronic characteristics among constituent elements, creates a favorable environment for the formation of structural defects accompanied by lattice distortions. Defects driven by compositional complexity can significantly influence the mean free paths of charge carriers, particularly electrons in metallic materials, thereby affecting the electrical conductivity of such systems [12, 13]. In this regard, multi-component alloys represent a promising platform for implementing the strategy of indirect defect engineering. The design and synthesis of such alloys inherently produce compositionally complex atomic environments, where atoms with diverse physical and electronic properties coexist within the same matrix. These environments act as driving forces for the formation of structural defects and lattice distortions during processes such as melting, solidification, and cooling. These thermophysical processes collectively govern the formation and evolution of defects, ultimately resulting in pre-engineered functional properties, most notably electrical conductivity. Recently, the eutectic Sn-Zn alloy system has attracted considerable attention, particularly because its melting temperature is close to that of the conventional Sn-Pb system, while avoiding the environmental and health concerns associated with lead. Consequently, Sn-Zn alloys have been considered a promising lead-free alternative for conventional solder materials [14,15]. When zinc (Zn), which is chemically more active, is added to the Sn-based material, distinct phase transformation characteristics are observed. Although the addition of Zn leads to the formation of Cu-Zn IMC layers (such as Cu_5Zn_8), the presence of free Zn; due to its high chemical activity; adversely affects wetting properties [16,17]. Despite this advantage, however, Sn-Zn alloys suffer from several intrinsic limitations, most notably their high susceptibility to oxidation and relatively poor wettability, which restrict their practical applicability. Furthermore, Zn alters corrosion mechanisms by acting as a ‘sacrificial galvanic anode’ within the less noble Sn matrix. Due to this active nature, non-protective, porous zinc chloride forms rapidly in salt solutions, thereby reducing the material’s durability [18–20]. To overcome the mechanical and environmental limitations of conventional binary matrices, modern alloy design strategies rely heavily on multicomponent solid solutions to engineer local phase stability and functional performance [21, 22]. Recent advances in near-eutectic lead-free systems, such as Sn-Zn-In configurations, demonstrate that multi-element addition effectively changes the thermodynamic properties of the melt [23]. Incorporating In alters the liquidus paths, depresses the overall melting temperature, and restructures initial solidification morphologies [21].

However, adding highly active alloying components complicates high-temperature oxidation behavior. Due to the high oxygen affinity of active elements like Zn and In, these alloys are highly prone to spontaneous surface scaling, forming restrictive oxide films (such as ZnO, In_2O_3, or mixed sub-oxides) that severely degrade wetting kinetics and service reliability [24]. Accordingly, significant efforts have been devoted to modifying the chemical composition of Sn-Zn alloys through alloying strategies aimed at improving their physicochemical and functional properties. In this context, the incorporation of additional alloying elements particularly indium (In) and antimony (Sb) into the Sn-Zn matrix has been widely explored, leading to the development of multicomponent Sn-Zn-In and Sn-Zn-Sb alloys that exhibit improved melting behavior and enhanced wettability [25–27]. The

introduction of indium into the Sn-Zn alloy matrix increases both the compositional and structural complexity of the system. In this regard, it has been reported that the electrical conductivity of eutectic Sn-Zn alloys decreases progressively with increasing indium content when used as a third alloying element. Specifically, when the indium concentration increased from 0.5 to 4.0 wt.%, the electrical conductivity decreased from 8.547×10^4 S/cm to 7.519×10^4 S/cm, indicating that increasing alloying content and compositional complexity is associated with a gradual deterioration in electrical conductivity [28]. Antimony (Sb) is often added to multi-component Sn alloys to enhance performance and improve thermal and mechanical stability. Its key characteristic is high solubility in both the matrix and the newly formed intermetallic compounds, which effectively prevents the formation of brittle phases. Compared to the active Sn-Zn binary system, the addition of Sb improves microstructural characteristics, creep properties, corrosion resistance, and wettability [29, 30]. A similar behavior has been observed in other multi-component tin-based alloy systems, such as ternary Sn-Ag-Cu (SAC) alloys. Although silver and copper possess some of the highest intrinsic electrical conductivities among metals, multi-element alloying leads to crystal lattice distortions, compositional inhomogeneity, and the formation of structural defects at both atomic and microstructural levels. These structural perturbations directly influence the electrical conductivity of the alloy as a metallic system [27, 28, 31]. The electrical conductivity of Sn-based alloys primarily depends on the mobility of electrons within the β-Sn matrix. Increasing compositional complexity promotes the formation of intermetallic compounds (IMCs), which constitute a major factor responsible for the deterioration of electrical transport performance due to their role as electron scattering centers [27,31]. Furthermore, rapid solidification conditions may lead to the formation of intermetallic phases such as Cu_3Sn and η-Cu_6Sn_5, while in Bi-Sn based systems, the addition of silver results in the formation of Ag_3Sn compounds through reactions between Ag and Sn. The formation of such IMCs has been associated with a reduction in electrical conductivity in these alloy systems [32–34].

Beyond their significant structural characteristics, the modern fabrication processes for the aforementioned multi-component alloys, particularly within the realm of electronic packaging, hold substantial real-world utility. Driven by stringent environmental regulations prohibiting the use of toxic lead in industrial applications, Sn-based alloys; such as Sn-Zn, Sn-Cu, and Sn-Ag-Cu; have emerged as the standard materials for lead-free substitution [27, 31]. Sn-Zn and other low-temperature solder alloys possess distinct thermal properties, rendering them ideally suited for use in sensitive aerospace electronics as well as in ‘through-hole’ technology components utilized in mainframe computers. Furthermore, SAC alloys are widely employed as solder pastes in semiconductor packaging, owing to their low melting points and superior electrical properties [27, 35]. Additionally, eutectic Sn-Cu alloys have been extensively utilized in automated ‘wave soldering’ processes for the production of printed circuit boards, as these alloys exhibit beneficial fluidity characteristics and are less prone to ‘hot cracking’. Research into Sn-Ag-Cu nano-solder alloy systems is also gaining momentum; these are currently being developed for future applications in microelectronics, primarily due to their low melting points [34, 36].

In the present work, two tin-based alloys, designated Sn-1 and Sn-2, were synthesized in order to provide a comparative evaluation of systems with different levels of compositional complexity. The Sn-1 alloy represents a near-eutectic binary Sn-Zn system containing a minor amount of lead, and is used here as a reference composition characterized by relatively simple chemical architecture. In contrast, the Sn-2 alloy represents a modified Sn-Zn system in which additional elements such as Cu, Sb, and Pb were incorporated, resulting in a

compositionally more complex alloy system. The investigated alloys were deliberately selected to represent two distinct levels of compositional complexity within Sn-based systems. Sn-1 was designed as a near-eutectic Sn-Zn alloy that serves as a compositionally simple reference material characterized by a relatively homogeneous microstructure and limited phase diversity. In contrast, Sn-2 was intentionally developed through the addition of Cu together with minor Sb and Pb contents (Pb addition occurred due to using Sn solder scraps) to create a compositionally complex alloy system. This comparative design enables systematic evaluation of how increasing compositional complexity influences phase evolution, microstructural heterogeneity, and electrical transport behavior [37, 38]. Despite extensive investigations into Sn-based solder alloys, most studies have primarily focused on improving mechanical performance, wettability, corrosion resistance, and thermal reliability through compositional modification. Comparatively little attention has been devoted to understanding how increasing compositional complexity itself affects structural evolution, lattice distortion, chemical heterogeneity, multiphase formation, all of which influence electrical transport behavior [39, 40]. Therefore, the present study addresses this knowledge gap by establishing a direct comparison between a near-eutectic Sn-Zn alloy and a compositionally complex Sn-Cu-Zn-Sb-Pb alloy, thereby providing new insights into the relationship between compositional complexity, phase evolution, and electrical conductivity. The present work does not seek to directly characterize crystallographic defects; rather, it examines how compositionally induced structural complexity contributes to the evolution of microstructural features that ultimately affect electrical conductivity. Through this comparative approach, the study seeks to evaluate the structural and electrical behavior of the investigated alloys, while also highlighting their potential applications beyond conventional soldering materials.

EXPERIMENTAL PROCEDURE

Alloy preparation

Two Sn-based alloys were synthesized via controlled melting–casting, with processing parameters deliberately adjusted to accommodate differences in elemental melting behavior and to ensure compositional homogeneity. High-purity Sn (99.9%) along with some Sn-based solder scraps and Zn (99.5%) served as base elements, while Cu (introduced as pre-cleaned industrial scrap) was incorporated in the multicomponent system. For Sn-1, Sn and Zn were melted in a preheated graphite crucible (500°C), followed by borax addition to limit oxidation and promote melt cleanliness. The alloy was stirred, cast, and rapidly quenched to retain a refined microstructure. For Sn-2, Sn and Zn were first melted at 500°C, after which Cu was introduced and the temperature raised to 750°C to ensure complete dissolution. Fluxing and stirring were maintained to enhance chemical uniformity. Casting into a preheated mold (200°C) followed by rapid quenching enabled preservation of the solidification structure. Post-solidification, both alloys were mechanically finished to achieve dimensional precision and surface integrity suitable for reliable characterization.

Elemental composition analysis of alloys

The bulk elemental composition of both alloys was determined using spark optical emission spectroscopy (Spark-OES), a reliable technique for quantitative analysis of major, minor, and trace elements in solid materials. The method is based on a high-energy electrical discharge that locally vaporizes and excites atoms at the sample surface, producing

characteristic spectral emissions for each element. The intensity of these emissions is directly proportional to elemental concentration. This approach enables direct, rapid, and minimally destructive compositional analysis without the need for chemical preparation, providing precise and reproducible data essential for accurate characterization of the investigated alloys [41–43].

Energy dispersive X-ray spectroscopy (EDS) was employed to estimate the local elemental composition, providing both qualitative and semi-quantitative information regarding the surface chemistry of the alloys. In addition, a scanning electron microscope (SEM, Model: 710HR) coupled with EDS (SEM-EDS) was utilized to investigate the spatial distribution of elements across the alloy surfaces through high-resolution elemental mapping [44, 45].

Surface microstructure and phases identification

Microstructural features were examined using high-resolution scanning electron microscopy (SEM, 710HR) to assess surface morphology across multiple magnifications [44]. Complementary phase identification was performed via X-ray diffraction (XRD, D6 PHASER), enabling precise detection of crystalline phases, including intermetallic and potential amorphous constituents within the alloy structure [46].

Electrical measurements

Electrical resistance was measured using the four-probe technique to eliminate contact resistance effects. A constant current was applied through the outer probes, while the voltage drops across the inner probes enabled precise resistance determination. Electrical resistivity (ρ) was calculated using $\rho = R \cdot A/L$ based on accurately measured sample dimensions, and conductivity (σ) was obtained as ($\sigma = 1/\rho$). The process was triplicated to ensure measurement reliability. The reported results indicate the arithmetic mean of the obtained measurements. This approach ensures high accuracy, reproducibility, and reliability in evaluating electrical transport behavior, making it particularly suitable for metallic and alloy systems [47].

RESULTS AND DISCUSSION

Elemental composition

Spark-OES analysis reveals a clear compositional contrast between the two alloys (Table 1), reflecting different levels of chemical complexity. Sn-1 contains twelve elements, yet is effectively binary, with Sn and Zn accounting for 99.9 wt.%. The remaining elements (Cu, Sb, Pb, Fe, Ni, In, Bi, As, Ge, Se) exist only at trace levels, confirming a chemically homogeneous, near-eutectic Sn–Zn system. In contrast, Sn-2 comprises fourteen elements and exhibits a pronounced compositional shift, most notably a reduction in Sn to 78.96 wt.% and a substantial increase in Cu to 11.2 wt.%, establishing it as a secondary major constituent. Zn remains constant (9.2 wt.%), while Sb and Pb appear as minor additions. Additional elements, including Ag and Cd, emerge at detectable levels, likely introduced via Cu feedstock or inherited from metallurgical impurities. This transition from near-binary to multicomponent composition signifies more than a quantitative change; it reflects a qualitative increase in compositional complexity. Such complexity inherently promotes chemical heterogeneity and provides a thermodynamic basis for defect generation and phase instability, underscoring its

critical role in governing subsequent microstructural evolution and functional behavior [48,49].

Table 1. *The elemental composition of alloys (wt%)*

Element	Sn	Zn	Cu	Sb	Pb	Fe	Ni	In	Bi	Ag	As	Cd	Ge	Se
Sn-1	90.70	9.20	0.003	0.016	0.040	0.014	0.001	0.003	0.005	--	0.004	--	0.006	0.001
Sn-2	78.96	9.20	11.20	0.315	0.192	0.087	0.005	0.003	0.006	0.001	0.003	0.002	0.012	0.001

The energy dispersive X-ray spectroscopy (EDS) spectrum and corresponding elemental maps of the Sn-1 alloy (Figs. 1 and 2) confirm that its surface composition is predominantly governed by tin (Sn) and zinc (Zn). The quantified surface concentrations of 59.93 wt.% for Sn and 16.75 wt.% for Zn (Table 2) align closely with the bulk compositional data, confirming chemical uniformity across the matrix. Trace amounts of sodium (Na) and ytterbium (Yb) were detected on the surface; however, their complete absence in the bulk analysis suggests they are incidental contaminants likely introduced during sample handling or from the surrounding environment.

Table 2. *EDS analysis for the elemental composition of Sn-1 alloy surface*

Element	Line	Mass%	Atom%
Sn	L	59.93 ± 0.69	33.97 ± 0.15
Zn	K	16.75 ± 0.44	17.24 ± 0.18
Na	K	15.12 ± 0.45	44.23 ± 0.51
Cd	L	6.51 ± 0.51	3.90 ± 0.12
Yb	M	1.69 ± 0.48	0.66 ± 0.07

Conversely, the detection of cadmium (Cd) on the surface, despite its absence in the bulk data, requires a different interpretation. Cadmium has a strong geochemical association with zinc ores, frequently substituting for Zn in the crystal lattice due to their highly similar atomic radii [48]. The localized surface enrichment of Cd is attributed to diffusion-driven atomic migration and surface segregation occurring during the high temperatures of melting and solidification. Consequently, Cd is interpreted as a geochemically inherited trace element originating from the zinc raw materials rather than as an external surface contaminant [48,50].

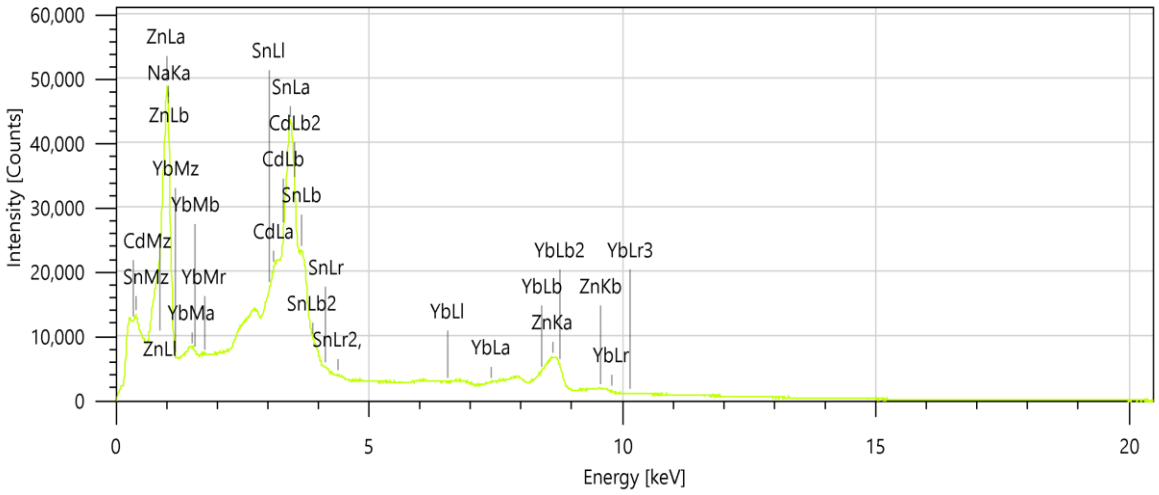


Fig. 1. Energy Dispersive X-ray (EDS) spectrum of the Sn-1 alloy showing the characteristic X-peaks of the principal alloying elements, Sn and Zn followed by Na, in addition to Cd and Yb

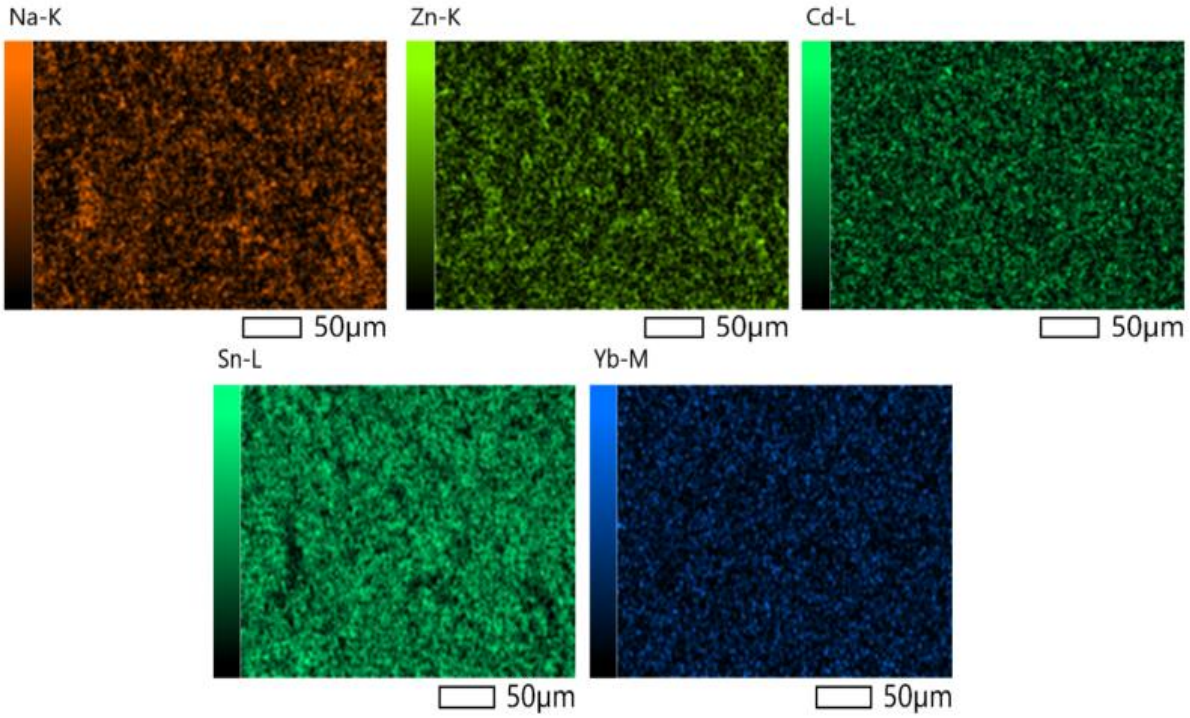


Fig. 2. SEM–EDS elemental mapping of the Sn-1 alloy presents the spatial elemental distribution maps of five elements (Sn, Zn, Na, Cd, and Yb) detected on the surface of the Sn-1 alloy. (1) The Sn-L map exhibits the strongest signal among all elements, confirming Sn as the dominant constituent at the surface. (2) The Zn-K signal is weaker than that of Sn, indicating Zn as a major alloying element secondary to tin. (3) The Na-K map shows a nearly homogeneous distribution, attributable to incidental surface contamination. (4) The Cd-L signal appears at low intensity with a relatively uniform distribution; Cd is an intrinsic constituent of the alloy, albeit at trace levels, consistent with its natural association with Zn in ores. (5) The Yb-M signal corresponds to ytterbium, which is not an intrinsic element of the Sn-1 alloy and is therefore ascribed to incidental surface contamination

For the more compositionally complex Sn-2 alloy, the EDS spectrum (Fig. 3) reveals a surface primarily composed of Sn, Zn, and Cd. The surface concentration of Sn was measured at 79.084 wt.%, demonstrating strong agreement with the bulk composition of 78.96 wt.%. The corresponding elemental map (Fig. 4) illustrates a highly uniform spatial distribution of Sn across the analyzed surface. Zinc, with a surface concentration of 10.58 wt.% (Table 3), exhibits a distinctly heterogeneous distribution pattern. Zinc appears in localized microscopic clusters, suggesting micro-scale compositional fluctuations and incipient phase separation within the alloy.

Table 3. *EDS analysis for the semi-quantitative determination of the elemental composition Sn-2 alloy*

Element	Line	Mass%	Atom%
Sn	L	79.84 ± 0.65	73.13 ± 0.37
Zn	K	10.58 ± 0.32	17.60 ± 0.33
Cd	L	9.58 ± 0.47	9.27 ± 0.28

Most notably, Cd displays a dramatic surface enrichment, measuring 9.58 wt.% compared to its bulk concentration of merely 0.002 wt.%. This significant discrepancy is best explained by pronounced diffusion-driven surface segregation. Unlike Zn, the Cd elemental map indicates that this enrichment is relatively uniform across the surface region. The complete absence of Na and Yb in the Sn-2 analysis provides further evidence that these elements were indeed incidental contaminants in the Sn-1 sample. Meanwhile, the persistent

surface detection of Cd in both alloys confirms its status as an inherent, geochemically inherited constituent of the alloy system derived from the zinc feedstock.

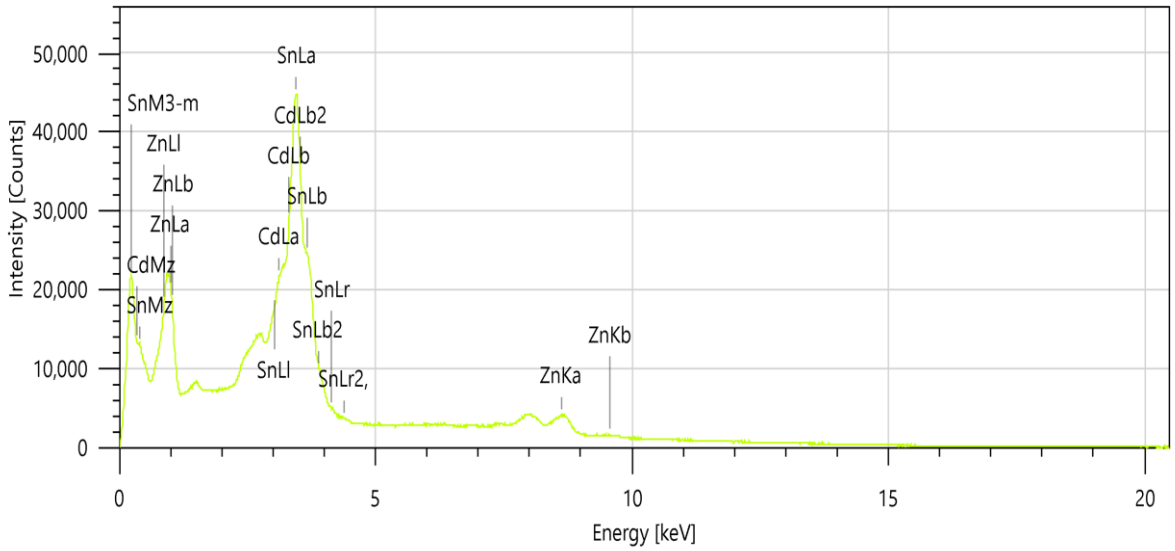


Fig. 3. Energy Dispersive X-ray (EDS) spectrum of the Sn-2 alloy showing the characteristic X-peaks of the principal alloying elements, Sn, Zn and Cd

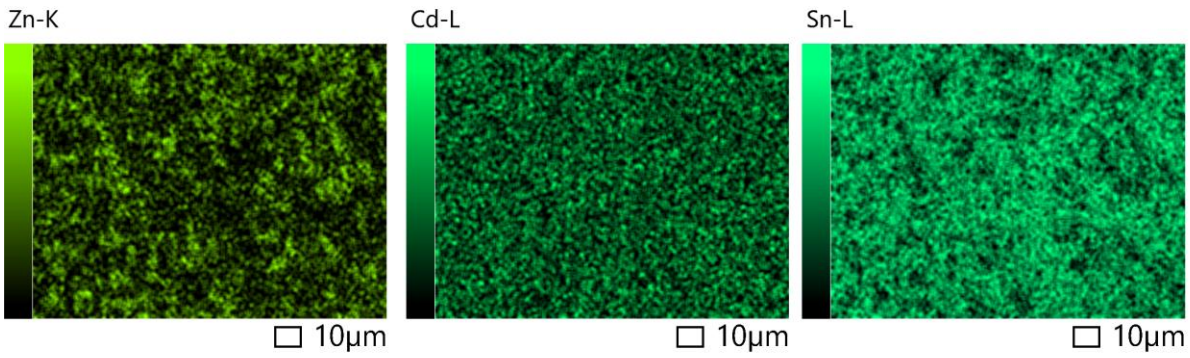


Fig. 4. The SEM–EDS elemental mapping of the Sn-2 alloy illustrates the spatial distribution maps of three elements, namely Sn, Zn, and Cd, detected on the alloy surface. (1) The Sn-L map exhibits the highest signal intensity among all detected elements, confirming that tin is the dominant constituent at the alloy surface. (2) The Zn-K signal is weaker than that of tin, indicating that zinc is the second most concentrated element at the surface after Sn. Zinc displays a non-homogeneous distribution in the form of localized agglomerations, giving rise to brighter regions interspersed with areas of lower brightness (darker regions). (3) The Cd-L signal appears at low intensity with a relatively uniform distribution; Cd is an intrinsic constituent of the alloy, albeit at trace levels, consistent with its natural association with Zn in ores

Microstructure and phases identification

The SEM micrographs of the Sn-1 alloy (Fig. 5) reveal a structurally coherent yet defect-mediated microstructure that requires interpretation in light of compositional data. At low magnification (Fig. 5A, ×1,100), the surface appears macroscopically homogeneous (~10 μm), but the presence of oriented striations and surface undulations indicates anisotropic solidification influenced by thermal gradients. The absence of visible grain boundaries or coarse phase segregation suggests that any compositional partitioning remains below the resolution limit. At higher magnification (Fig. 5B, ×27,000), lamellar-like features and nanoscale roughness (~500 nm) become evident. The lack of pores or cracks confirms good

structural integrity, yet these fine features indicate that internal stresses are accommodated through subtle microstructural adjustments. Correlation with EDS maps (Fig. 4) shows uniform distributions of Sn, Zn, and Cd over ~50 μm, excluding coarse chemical segregation. Thus, Zn is likely incorporated substitutionally within the Sn matrix or as unresolved fine phases. Cd, despite its low concentration (Table 1), also appears uniformly distributed and is plausibly incorporated due to its geochemical association with Zn [51]. Accordingly, the observed morphology is primarily structural rather than chemical in origin, reflecting intrinsic crystallographic defects such as substitutional atoms, vacancies, and dislocations. These defects accommodate atomic size mismatch and solidification stresses while maintaining overall compositional homogeneity. Functionally, they act as electron-scattering centers, reducing conductivity relative to pure Sn, though the absence of macroscopic phase boundaries limits severe transport disruption. In contrast, the SEM micrographs of Sn-2 (Fig. 6) reveal a markedly more complex microstructure, consistent with its multicomponent nature. At low magnification (Fig. 6A, ×2,000), the surface appears superficially homogeneous but exhibits irregular topography and a high density of elongated needle-like (acicular) features within a brighter Sn-rich matrix. This morphology indicates multiphase solidification rather than a simple solid solution. Additionally, pores and microcracks are observed, likely arising from solidification shrinkage and thermal mismatch between phases. At intermediate magnification (Fig. 6B, ×9,000), the acicular structures appear more interconnected, suggesting cooperative growth. Localized micro-voids and strong topographical contrast indicate phase heterogeneity. At higher magnifications (Fig. 6C-D, ×14,000-30,000), the structure evolves into a dense network of submicron to nanoscale needle-like precipitates. The absence of coarse particles indicates that compositional complexity is accommodated through finely dispersed phases rather than large-scale segregation. Correlation with EDS maps (Fig. 4), Spark-OES and XRD results confirms that these acicular features correspond to Zn-Cu intermetallic phases; i.e. γ Cu_5Zn_8, rather than elemental Zn.

Although a distinct copper (Cu) peak was not observed using the microscopic localized EDS technique, the total chemical composition determined by the macroscopic Spark-OES technique confirmed the presence of Cu (11.2wt%) and Zn (9.2wt%) in the alloy. The above variance is direct proof of intense metallurgical scavenging due to a strong affinity between Cu and Zn and hence the segregation of Cu from the solid solution due to precipitation. This leaves the surrounding Sn matrix devoid of any traces of Cu that can be detected using EDS. The XRD pattern clearly revealed the presence of the cubic γ Cu_5Zn_8 phase. Thermodynamically, the Gibbs energy of formation for Cu-Zn intermetallic compounds is significantly lower (more negative) than that of the Cu-Sn system. Thermodynamically the formation of γ Cu_5Zn_8 is more favored than the formation of standard Cu_6Sn_5. The resulting high-density internal phase boundaries enhance carrier scattering and significantly reducing the electron mean free path, thereby explaining the low electrical conductivity of the Sn-2 matrix. Thus, the electrical behavior of Sn-2 is governed not only by composition but by its complex microstructural architecture. Overall, the combined analysis of SEM (Figs. 5-6), EDS (Fig. 4), and compositional data (Table 1) demonstrates a transition from a chemically homogeneous, defect-controlled structure in Sn-1 to a structurally complex, multiphase system in Sn-2. This evolution reflects indirect defect engineering, where increased compositional complexity intrinsically drives defect formation and phase evolution, ultimately governing the structural and electrical performance of the alloys.

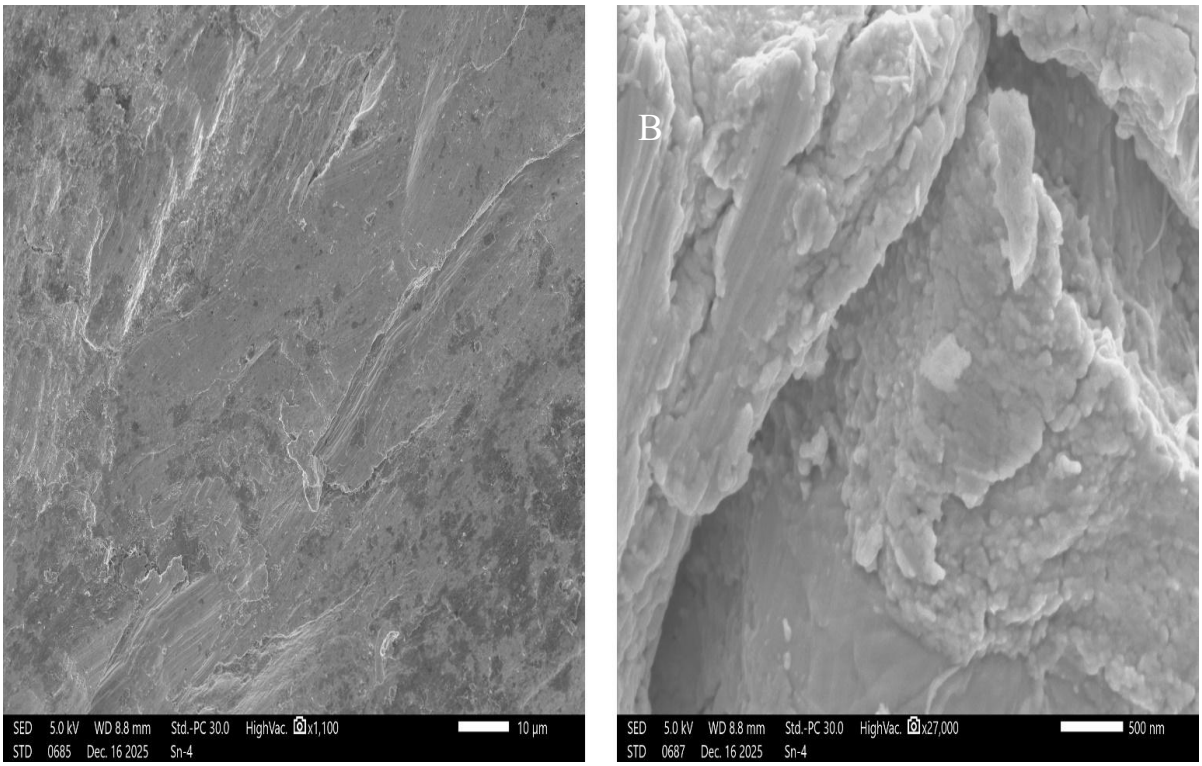


Fig. 5. SEM micrographs of the Sn-1 alloy surface at two different magnifications: (A) low magnification (×1100, scale bar = 10 µm) showing a relatively homogeneous surface matrix intersected by elongated striations and surface undulations without evident macro-scale phase segregation; (B) high magnification (×27,000, scale bar = 500 nm) revealing refined lamellar-like features and localized surface roughness, indicating fine microstructural modulation in the absence of observable microcracks or large voids

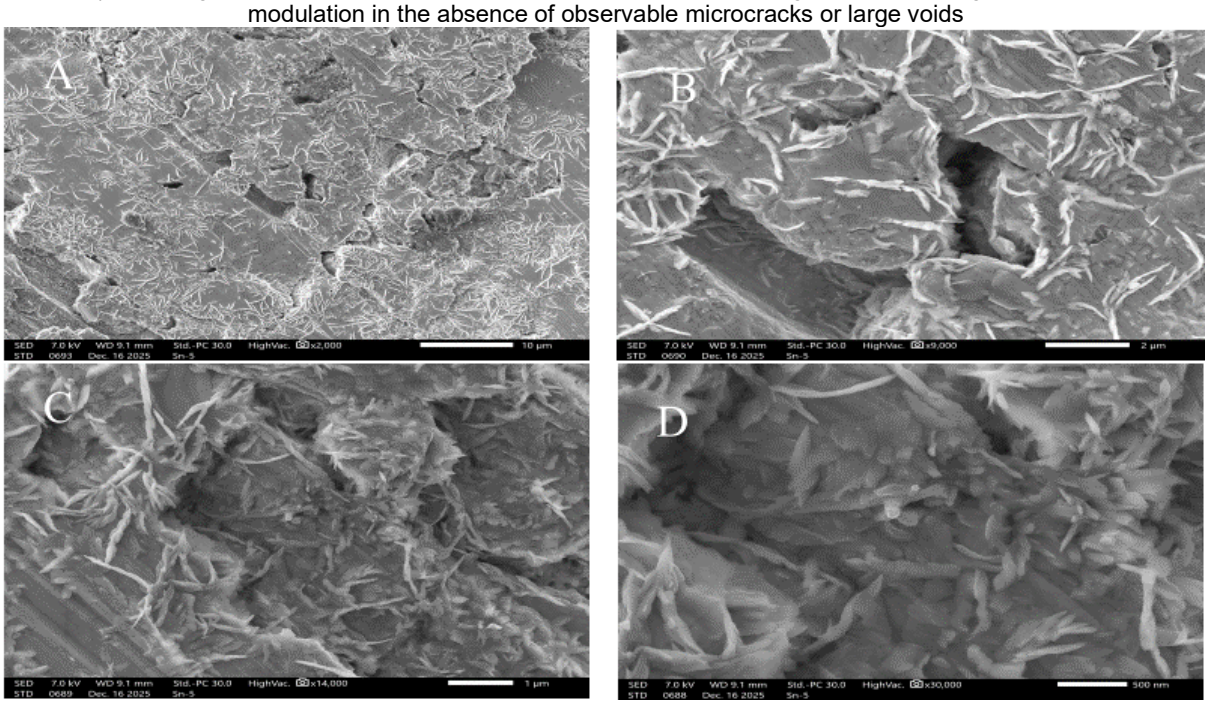


Fig. 6. SEM micrographs of the Sn-2 alloy at different magnifications showing the progressive refinement of the microstructure. (A) ×2,000 (10 µm): general surface morphology with a continuous matrix containing densely distributed acicular features and scattered micro-voids. (B) ×9,000 (2 µm): clearer needle-like/plate-like morphology with anisotropic growth and a localized cavity. (C) ×14,000 (1 µm): interwoven submicron acicular structures embedded within the matrix. (D) ×30,000 (500 nm): highly refined nanoscale lamellar/acicular features with high aspect ratio and increased interfacial density

The X-ray diffraction (XRD) patterns of Sn-1 and Sn-2 alloys (Figs. 7-8) exhibit clear deviations from the reference pattern of pure β-Sn, providing direct evidence of alloying-induced structural modification. Pure tin is characterized by well-defined reflections corresponding to its tetragonal structure (Table 4), whereas both alloys show peak shifts indicative of changes in interplanar spacing due to solute incorporation. For Sn-1, peak shifts remain limited (≈0.03°–0.27°), with one anomalous shift (~0.80° for the (400) plane), suggesting minor lattice distortion consistent with a substitutional solid solution. The persistence of β-Sn as the dominant phase, alongside minor additional peaks attributed to Zn-containing phases, indicates that structural modification is primarily distortion-driven rather than phase-transformative. In contrast, Sn-2 exhibits more pronounced peak shifts (≈0.04°-1.05°), reflecting stronger lattice perturbation due to increased compositional complexity. More critically, the emergence of additional diffraction peaks confirms the formation of secondary phases, notably the intermetallic Cu_5Zn_8. This phase originates from Cu-Zn interactions during high-temperature processing and appears as distinct reflections, marking a transition from single-phase to multiphase behavior. Correlation with SEM morphology (Fig. 6) and Zn distribution (Fig. 4) supports that the observed needle-like features correspond to Cu_5Zn_8, representing a morphology evolution from the rod-like structures reported previously, driven by directional solidification. Additionally, weak peaks indexed to $CoFe_2O_4$ suggest the formation of oxide phases arising from trace impurities (Co, Fe) inherited from raw materials and activated during processing. Peak shifts were quantified using: $\Delta 2\theta = 2\theta_{Alloy} - 2\theta_{Sn}$, where deviations reflect lattice distortion, solute incorporation, or phase formation. Overall, Sn-1 demonstrates distortion-dominated behavior, whereas Sn-2 reveals a structurally evolved, multiphase system governed by intermetallic formation and impurity-driven reactions, highlighting the critical role of compositional complexity in indirect defect generation and phase stability.

Table 4. *Shifts in X-ray diffraction (XRD) peak positions for multi-component tin-based alloys (Sn-1 and Sn-2) relative to pure tin, highlighting the impact of compositional complexity on the formation of lattice defects and crystallographic distortions*

Crystallographic Plane (*hkl*)	Pure Sn (2θ°)	Sn-1 (2θ°)	$\Delta 2\theta$ Sn-1	Sn-2 (2θ°)	$\Delta 2\theta$ Sn-2
(200)	30.63	30.90	+ 0.27	30.40	− 0.23
(101)	32.00	31.80	− 0.20	32.92	+ 0.92
(220)	43.88	43.91	+ 0.03	43.01	− 0.87
(211)	44.90	44.79	− 0.11	44.21	− 0.69
(301)	55.32	55.19	− 0.13	55.36	+ 0.04
(112)	62.54	62.30	− 0.24	62.59	+ 0.05
(400)	63.84	64.64	+ 0.80	64.89	+ 1.05
(321)	72.44	72.60	+ 0.16	72.91	+ 0.47
(420)	79.33	79.24	− 0.09	79.48	+ 0.15
(411)	81.55	81.80	+ 0.25	81.97	+ 0.42

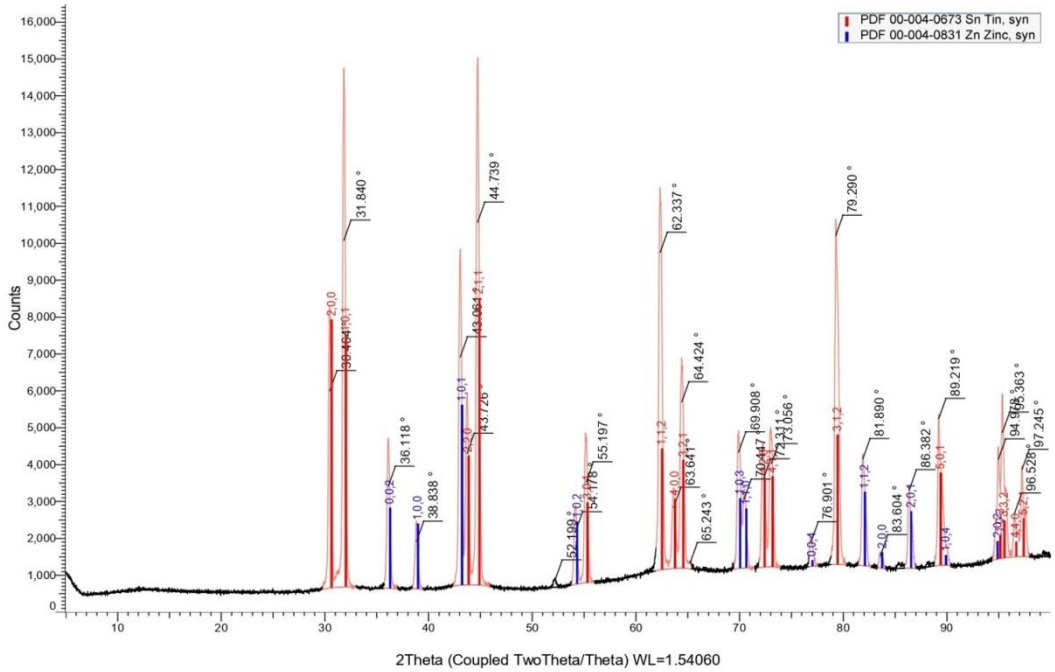


Fig. 7. X-ray diffraction (XRD) pattern of the Sn-1 alloy showing a fully crystalline structure composed of two distinct phases: β-Sn (tetragonal) and Zn (hexagonal). The sharp and high-intensity diffraction peaks confirm a high degree of crystallinity

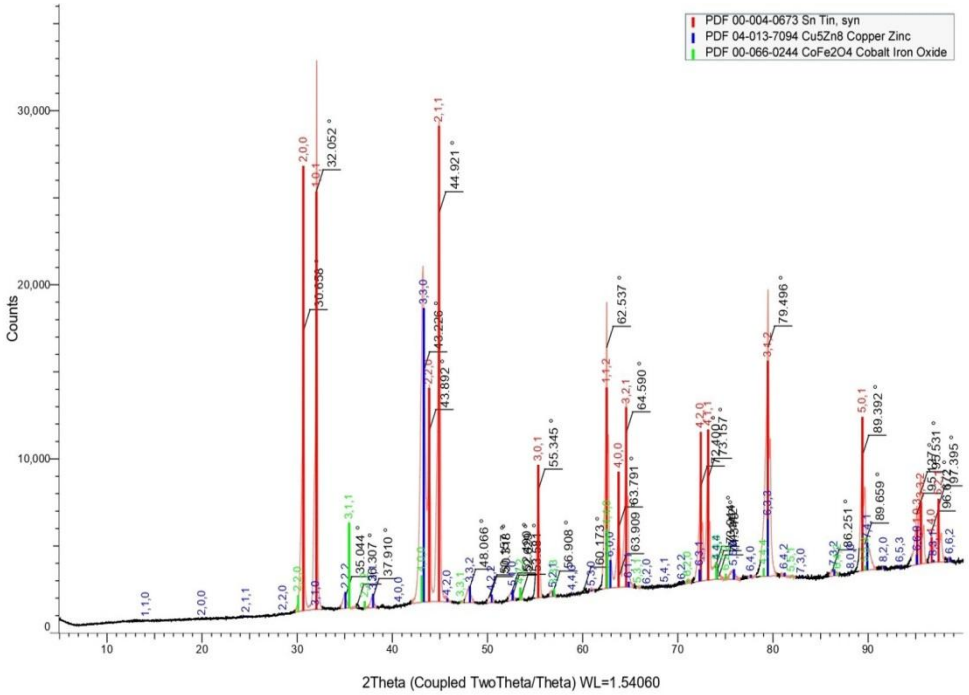


Fig. 8. X-ray diffraction (XRD) pattern of the Sn-2 alloy revealing a multiphase crystalline structure composed of a dominant tetragonal *β*-Sn matrix, intermetallic Cu_5Zn_8 (cubic), and a secondary $CoFe_2O_4$ phase (cubic).

Compositionally driven structural defects

Atomic size (radius) is a governing parameter in defining lattice structure, physically linked to electron density distribution around atoms. In multicomponent alloys (Sn-1, Sn-2), its role extends beyond simple size differences (Table 1) to include electronic constraints such as Pauli repulsion, which drive atoms away from ideal lattice sites. This complexity is quantified using the atomic size mismatch parameter (δ), which measures deviation from the mean atomic radius and serves as a statistical indicator of lattice distortion and defect propensity.

$$\delta = \sqrt{\sum_i^n c_i \,(1 - \frac{r_i}{\bar{r}})^2}, \bar{r} = \sum_i^n c_i \, r_i$$

The calculated δ values reveal distinct structural regimes: Sn-1 exhibits a low δ = 2.47% (Table 5), consistent with near-ideal solid solution behaviour, whereas Sn-2 shows a significantly higher δ = 6.6% (Table 6), indicating pronounced lattice distortion. This increase reflects not merely a quantitative change but a qualitative transition toward collective, interacting distortions driven by atomic size disparity. Accordingly, δ captures the essence of indirect defect engineering, where compositional complexity induces interconnected lattice perturbations and defect networks, rather than isolated point defects.

Table 5. *Calculation of atomic fractions, mean atomic radius, and lattice distortion contributions for the Sn-1 alloy, showing the elemental contributions* $c_i \left(1 - \frac{r_i}{\bar{r}}\right)^2$ *used to quantify lattice distortion arising from compositional complexity*

Element	Atomic mass	Atomic radii	Sn-1				
	(M)	(Å)	Wt.%	$\frac{w_i}{M_i}$	$c_i = \frac{w_i/M_i}{\sum w_i/M_i}$	$c_i r_i$	$c_i \left(1 - \frac{r_i}{\bar{r}}\right)^2$
Sn	118.71	1.8732	90.700	0.764	0.848	1.589	0.00001
Zn	65.38	1.8004	9.200	0.141	0.156	0.281	0.0001
Cu	63.55	1.648	0.003	0.00005	0.00005	0.00008	0
Sb	121.76	1.6799	0.016	0.00013	0.00014	0.00023	0
Pb	207.2	2.3603	0.040	0.00019	0.00021	0.00050	0.0002
Fe	55.85	2.0885	0.014	0.00025	0.00028	0.00058	0.0001
Ni	58.69	1.9337	0.001	0.00002	0.00002	0.00004	0
In	114.82	2.1167	0.003	0.00003	0.00003	0.00006	0
Bi	208.98	2.1167	0.005	0.00002	0.00002	0.00005	0
Ag	107.87	2.5199	----	----	----	----	----
As	74.92	1.2431	0.004	0.00005	0.00005	0.00006	0.0001
Cd	112.41	2.433	----	----	----	----	----
Ge	72.63	1.3862	0.006	0.00008	0.00009	0.00012	0.0001
Se	78.97	1.1269	0.001	0.00001	0.00001	0.00001	0
∑				**0.90554**		$\bar{r}$ **=1.87173**	**0.00061**

Table 6. *Calculation of atomic fractions, mean atomic radius, and lattice distortion contributions for the Sn-2 alloy, showing the elemental contributions* $c_i\left(1-\frac{r_i}{\bar{r}}\right)^2$ *used to quantify lattice distortion arising from compositional complexity*

Element	Atomic mass	Atomic radii	Sn-2				
	(M)	(Å)	Wt.%	$\frac{w_i}{M_i}$	$c_i=\frac{w_i/M_i}{\sum w_i/M_i}$	$c_i r_i$	$c_i\left(1-\frac{r_i}{\bar{r}}\right)^2$
Sn	118.71	1.8732	73.960	0.665	0.659	1.235	0.0006
Zn	65.38	1.8004	9.200	0.141	0.140	0.252	0.0002
Cu	63.55	1.648	11.200	0.176	0.175	0.288	0.0025
Sb	121.76	1.6799	0.315	0.0026	0.0026	0.0044	0.00001
Pb	207.2	2.3603	0.192	0.00093	0.0009	0.0021	0.0004
Fe	55.85	2.0885	0.087	0.00156	0.0015	0.0031	0.0003
Ni	58.69	1.9337	0.005	0.00009	0.00009	0.00017	0.00005
In	114.82	2.1167	0.003	0.00003	0.00003	0.00006	0
Bi	208.98	2.1167	0.006	0.00003	0.00003	0.00006	0
Ag	107.87	2.5199	0.001	0.00001	0.00001	0.00003	0
As	74.92	1.2431	0.003	0.00004	0.00004	0.00005	0.0001
Cd	112.41	2.433	0.002	0.00002	0.00002	0.00005	0
Ge	72.63	1.3862	0.012	0.00017	0.00017	0.00024	0.0002
Se	78.97	1.1269	0.001	0.00001	0.00001	0.00001	0
∑				**0.98749**		$\bar{r}$ **=1.78527**	**0.00436**

Electrical Conductivity Response to Compositional Complexity and Structural Defects

The integrated analysis of composition (Spark-OES), microstructure (SEM), elemental mapping (SEM-EDS), phase constitution (XRD), and lattice distortion (δ) demonstrates that electrical conductivity in Sn-based alloys is a defect-mediated response to compositional complexity rather than an intrinsic property. In Sn-1, the near-binary composition (99.9 wt.% Sn-Zn) and low δ (2.47%, Table 5) correspond to minimal lattice distortion, confirmed by slight XRD peak shifts ($\Delta 2\theta \approx 0.03$-$0.27°$) and absence of new phases. SEM and EDS (Fig. 4, Fig. 5) reveal chemical homogeneity and a defect structure limited to weak point and line defects, preserving long electron mean free paths and high conductivity (1.105×10^5 S/cm). Conversely, Sn-2 exhibits a compositional shift (Cu ≈ 11.2 wt.%) and elevated δ (6.6%, Table 6), marking a transition to a distortion-dominated regime. XRD (Figs. 7-8) confirms multiphase formation (Cu_5Zn_8, $CoFe_2O_4$), while SEM (Fig. 6) and EDS (Fig. 4) reveal micro-segregation and dense interfacial networks. These features generate multidimensional scattering centers, reducing conductivity to 8.097×10^4 S/cm (Table 7).

This behavior exemplifies indirect defect engineering, where compositional complexity systematically governs electron transport. Within metallic alloy systems, compositional complexity can promote lattice distortion, chemical heterogeneity, and multiphase formation all of which can influence the electrical behavior. As the measurements reveal the multi-element Sn-2 exhibits a significant reduction in conductivity compared to the baseline binary Sn-1 alloy. This sharp decline directly validates the defect engineering strategy. The transition from a simple binary system to a multi-element matrix drastically increases the local compositional complexity, which inherently induces severe lattice distortion and a higher density of point defects. The calculated lattice distortion parameter (δ) provides a quantitative

measure of the structural perturbation introduced by compositional complexity. The higher δ value (6.6%) obtained for Sn-2 indicates increased atomic-size mismatch and local lattice distortion, which are expected to enhance electron scattering and contribute directly to the observed reduction in electrical conductivity. These engineered defect formations act as potent scattering centers for charge carriers. The severe disruption of the periodic lattice potential increases carrier scattering, thereby directly causing the observed reduction in conductivity.

Table 7. *The fundamental electrical characteristics of Sn-based alloys*

Alloy	Composition	R (Ω)	ρ (Ω. cm)	σ (S/cm)
Sn-1	Sn-Zn	1.12×10^{-4}	9.0517×10^{-6}	1.105×10^{5}
Sn-2	Sn-Cu-Zn-Sb-Pb	1.18×10^{-4}	1.235×10^{-5}	8.097×10^{4}

The reduction in electrical conductivity observed in Sn-2 can be partly attributed to the formation of additional intermetallic phases, particularly Cu_5Zn_8, identified by XRD analysis. These intermetallic constituents introduce numerous phase boundaries and chemically heterogeneous regions that act as effective electron-scattering centres. Consequently, the electron mean free path becomes progressively restricted, leading to increased resistivity and lower conductivity relative to the simpler Sn-1 alloy. The influence of interfacial scattering is further amplified by the multiphase nature of Sn-2, which promotes discontinuities in the electronic transport pathway.

Quantitative evaluation of microstructural evolution and defect-mediated electrical conductivity

The reduction in conductivity can further be supported by X-ray Line Profile Analysis (XLPA) using Williamson-Hall method. Utilizing the Williamson-Hall method, the total Bragg peak broadening β was deconvoluted into its constituent components of crystallite size D and lattice micro-strain ε via the relation,

$$\beta \cos(\theta) = \frac{K\lambda}{D} + 4\,\varepsilon \sin(\theta)$$

Where:
β = Full Wave at Half Maximum-FWHM (in Radians)
θ = Bragg Angle or Diffraction Angle
K = Scherrer Constant (taken as 0.9)
D = Crystallite Size
λ = X-Ray Wavelength (*Cu-Kα* = 0.15406 nm) and
ε = Lattice Micro-strain

Analysis of the broadening of the diffraction peak reveals that, compared to the binary alloy, the multi-element Sn-2 alloy exhibits an increase in coherent crystallite size (D) alongside an increase in lattice micro-strain (ε) (Table 8).

Table 8. *X-Ray Line Profile Analysis (XLPA) for Micro-strain and Crystallite Size Calculation of Sn-based Alloys*

Alloy	Lattice Micro-strain (ε)	Crystallite Size (D)
Sn-1	8.23499×10^{-5}	25.579 nm
Sn-2	8.15×10^{-4}	62.237 nm

The structural refinement (increased D) confirms that the combination of high solute concentration and rapid thermodynamic precipitation of the acicular γ Cu_5Zn_8 phase effectively clears the intervening β-Sn matrix spaces of chaotic, random solid-solution solutes through elemental scavenging. This allows the remaining localized tin domains to grow cleanly and continuously between the intermetallic needles. While increased crystallite size indicates reduction in lattice distortion, the significant increase in ε combined with formation of γ Cu_5Zn_8 acicular phase strongly dominates the system and hence increases lattice distortion. Such internal strain fields arise from the large atomic radius mismatch between the host Sn matrix and the high-concentration Cu, Zn, and Sb solutes; a fact confirmed by bulk Spark-OES measurements. In the context, these parameters offer a quantitative description of the fundamental mechanisms altering transport properties: bigger crystallites decrease the density of internal sub-grain boundaries, while elevated micro-strain severely distorts the lattice potential. This extreme lattice distortion heavily disrupts the periodic lattice potential, serving as the primary physical mechanism that reduces the electron mean free path and drives down the electrical conductivity of the Sn-2 alloy.

Table 9. *Comparison of the electrical conductivity values of the investigated Sn-based alloys with similar lead-free solder systems in literature [35,52–54]*

Alloy System (wt.%)	Electrical Conductivity (% IACS)	Electrical Conductivity (MS/m)	Reference
High Conductivity Baseline			
Pure Sn (β-Sn)	~15	~8.7	Standard Reference
$Sn_{3.0}Ag_{0.5}Cu$ (SAC305)	15.28	8.88	[35]
Sn-1	19.02	11.05	This Work
Multi-element System			
Sn-2	13.93	8.097	This Work
$Sn_{3.0}Ag_{0.5}Cu_{1.0}Zn_{1.0}Bi$	13.75	7.99	[35]
$Sn_9Zn_4Bi_1Sb$	12.20	7.08	{52]
Low Conductivity Eutectic/ Near Eutectic System			
$Sn_{37}Bi$	5.97	3.47	[54]
$Sn_{57}Bi$	3.41	1.98	[54]
$Sn_{94.9}Ag_{3.8}Cu_{1.3}$	4.7	2.73	[53]
$Sn_{98.7}Cu_{1.3}$	4.51	2.62	[53]

The results regarding the conductivity performance and transport properties of the new alloys are compared in Table 9 with those of other multi-component Pb-free solder systems. For the binary alloy Sn-1, the conductivity is 19.02 % IACS, which is comparable to the typical conductivity reported for pure Sn and SAC305 alloys. However, for the multi-element alloy Sn-2, the conductivity drops significantly to 13.93 % IACS. A comparison of this value with existing literature indicates that this substantial reduction in transport performance is consistent with the characteristics of significantly modified lead-free solders. For instance, Kang et al. observed a ~10% decrease in conductivity upon adding Zn to the SAC system

[35], attributed to the formation of intermetallic phases. Another study by Ata Esener et al. found that the addition of Sb to a zinc-containing tin matrix resulted in a significant reduction due to intense carrier scattering [52].

In particular, the significant reduction observed in the Sn-2 alloy is noteworthy because the substantial solute content (11.2 wt.% Cu and 9.2 wt.% Zn) causes a large portion of the matrix phase to transform into the denser cubic acicular γ Cu_5Zn_8 structure. Due to the higher lattice micro-strain (ε) revealed by our Williamson-Hall study, the effect of carrier scattering is much more pronounced in this alloy compared to typical low-solute ternary alloys.

CONCLUSION

Electrical conductivity in Sn-based alloys emerges as a defect-governed property rather than an intrinsic characteristic of the base metal. The transition from Sn-1 to Sn-2 reflects a shift from a structurally coherent, low-distortion matrix to a highly heterogeneous system dominated by lattice strain, phase multiplicity, and micro-segregation. While Sn-1 preserves efficient electron transport through minimal defect density, Sn-2 introduces multidimensional scattering centers that suppress carrier mobility. The conductivity reduction is therefore not a loss of crystallinity but a transformation in defect architecture. The present results demonstrate that increasing compositional complexity (δ = 2.47% for Sn-1 to δ = 6.6% for Sn-2) promotes lattice distortion, phase diversification, and microstructural heterogeneity, all of which contribute to changes in electrical transport behavior. These findings underscore compositional complexity as a primary driver of defect formation and validate indirect defect engineering as a strategic pathway for tuning electrical performance. Nevertheless, direct characterization of crystallographic defects requires advanced techniques (like, CALPHAD assisted alloy design framework) and remains an important direction for future investigations.

ACKNOWLEGEMENT

The authors would like to acknowledge the Department of Chemistry, Gujarat University, Navrangpura, Ahmedabad, India for providing the lab facilities and necessary supports. The authors Mostafa M. Basheir, Meki K. Bedasa and Biplob Sen would like to acknowledge Indian Council for Cultural Relations (ICCR) for fellowship.

Conflict of interest
The authors declare no conflict of intertest.
Funding
The authors did not receive any external funding for this research.
Ethics approval
This work is original, has not been published previously and is not under consideration elsewhere.

REFERENCES

1. Tripathy SR, Baral SS. Defect Engineering in Semiconductor Photocatalysts: Enhancing Photocatalytic Activity for Green Energy Production. Adv Energy Sustain Res. 2025 Nov;6(11):2500110. doi:10.1002/aesr.202500110

2. Luo Y, Wu Y. Defect Engineering of Nanomaterials for Catalysis. Nanomaterials. 2023 Mar 21;13(6):1116. doi:10.3390/nano13061116

3. Benton JL, Libertino S, Kringho/j P, Eaglesham DJ, Poate JM, Coffa S. Evolution from point to extended defects in ion implanted silicon. J Appl Phys. 1997 Jul 1;82(1):120–5. doi:10.1063/1.365583

4. Luo Y, Wu Y, Huang C, Menon C, Feng S, Chu PK. Plasma modified and tailored defective electrocatalysts for water electrolysis and hydrogen fuel cells. EcoMat. 2022 Jul;4(4):e12197. doi:10.1002/eom2.12197

5. Song G, Cong S, Zhao Z. Defect engineering in semiconductor-based SERS. Chem Sci. 2022;13(5):1210–24. doi:10.1039/D1SC05940H

6. Ma J, Long R, Liu D, Low J, Xiong Y. Defect Engineering in Photocatalytic Methane Conversion. Small Struct. 2022 Jan;3(1):2100147. doi:10.1002/sstr.202100147

7. Liu J, Wei Z, Shangguan W. Defects Engineering in Photocatalytic Water Splitting Materials. ChemCatChem. 2019 Dec 18;11(24):6177–89. doi:10.1002/cctc.201901579

8. Liu J, Wei Z, Shangguan W. Defects Engineering in Photocatalytic Water Splitting Materials. ChemCatChem. 2019 Dec 18;11(24):6177–89. doi:10.1002/cctc.201901579

9. Nowotny J, Alim MA, Bak T, Idris MA, Ionescu M, Prince K, et al. Defect chemistry and defect engineering of TiO_2 -based semiconductors for solar energy conversion. Chem Soc Rev. 2015;44(23):8424–42. doi:10.1039/C4CS00469H

10. Schuler B, Lee JH, Kastl C, Cochrane KA, Chen CT, Refaely-Abramson S, et al. How Substitutional Point Defects in Two-Dimensional WS_2 Induce Charge Localization, Spin–Orbit Splitting, and Strain. ACS Nano. 2019 Sep 24;13(9):10520–34. doi:10.1021/acsnano.9b04611

11. Gajaria TK, Roondhe B, Dabhi SD, Śpiewak P, Kurzydłowski KJ, Jha PK. Hydrogen evolution reaction electrocatalysis trends of confined gallium phosphide with substitutional defects. Int J Hydrog Energy. 2020 Sep;45(44):23928–36. doi:10.1016/j.ijhydene.2019.09.032

12. Chen Q, Yang C, Xing T, Xi J, Zhang W, Yang J, et al. Defect engineering and alloying strategies for tailoring thermoelectric behavior in GeTe and its alloys. J Materiomics. 2025 Jan;11(1):100832. doi:10.1016/j.jmat.2024.01.007

13. Zheng Y, Slade TJ, Hu L, Tan XY, Luo Y, Luo ZZ, et al. Defect engineering in thermoelectric materials: what have we learned? Chem Soc Rev. 2021;50(16):9022–54. doi:10.1039/D1CS00347J

14. Zhang L, Xue S bai, Gao L li, Sheng Z, Ye H, Xiao Z xiang, et al. Development of Sn–Zn lead-free solders bearing alloying elements. J Mater Sci Mater Electron. 2010 Jan;21(1):1–15. doi:10.1007/s10854-009-0014-1

15. Suganuma Katsuaki, Kim KSoo. Sn-Zn low temperature solder. In: Lead-Free Electronic Solders [Internet]. Boston, MA: Springer US; 2007 [cited 2026 May 26]. p. 121–7. Available from: http://link.springer.com/10.1007/978-0-387-48433-4_7 doi:10.1007/978-0-387-48433-4_7

16. Zhao M, Zhang L, Liu ZQ, Xiong MY, Sun L. Structure and properties of Sn-Cu lead-free solders in electronics packaging. Sci Technol Adv Mater. 2019 Dec 31;20(1):421–44. doi:10.1080/14686996.2019.1591168

17. Yu DQ, Xie HP, Wang L. Investigation of interfacial microstructure and wetting property of newly developed Sn–Zn–Cu solders with Cu substrate. J Alloys Compd. 2004 Dec;385(1–2):119–25. doi:10.1016/j.jallcom.2004.04.129

18. Yu DQ, Xie HP, Wang L. Investigation of interfacial microstructure and wetting property of newly developed Sn–Zn–Cu solders with Cu substrate. J Alloys Compd. 2004 Dec;385(1–2):119–25. doi:10.1016/j.jallcom.2004.04.129

19. Mohamed HS, Mostafa MM, Mahmoud NM. Crystallographic, microstructure, electrical, and hardness characterization of advanced Sn-9Zn-0.5ZrO2 and Sn-9Zn-xNi lead-free solder alloys. J Mater Sci Mater Electron. 2025 May;36(13):784. doi:10.1007/s10854-025-14760-9

20. Xiao J, Tong X, Liang J, Chen Q, Tang Q. Microstructure and morphology of the soldering interface of Sn–2.0Ag–1.5Zn low Ag content lead-free solder ball and different substrates. Heliyon. 2023 Feb;9(2):e12952. doi:10.1016/j.heliyon.2023.e12952

21. Al-Ezzi AS, Kader Ekhlas, Alazzawi S. Effect of alloying elements on microstructural and electrical property in Sn–Cu–Bi lead-free solder alloys. Weld Int. 2024 Mar 3;38(3):211–24. doi:10.1080/09507116.2024.2317322

22. Arı M, Aksöz S, Ata Esener P, Öztürk E. Thermal, electrical, and mechanical properties of Sn-Ag-Zn solder alloys for BGA packaging. Phys B Condens Matter. 2025 Feb;699:416868. doi:10.1016/j.physb.2024.416868

23. Villarreal-Loya RE, Garay-Reyes CG, Mendoza-Duarte JM, Hernández-Rivera JL, Cruz-Rivera JJ, Estrada-Guel I, et al. Ultra-low-temperature lead-free multicomponent alloy solder for application in heat-sensitive electronic components. Mater Lett. 2023 Jul;343:134342. doi:10.1016/j.matlet.2023.134342

24. Sun Q, Liao X, Dai J, Feng W, Zhang L, Yin L. Recent Advances in Sn-Based Lead-Free Solders for Electronic Packaging: A Review [Internet]. In Review; 2025 [cited 2026 Jul 1]. Available from: https://www.researchsquare.com/article/rs-8100930/v1 doi:10.21203/rs.3.rs-8100930/v1

25. Fima P, Gancarz T, Pstruś J, Sypień A. Wetting of Sn-Zn-xIn (x = 0.5, 1.0, 1.5 wt%) Alloys on Cu and Ni Substrates. J Mater Eng Perform. 2012 May;21(5):595–8. doi:10.1007/s11665-012-0124-4

26. Xie X, Lin P, Lian B, Xu S, Wang Y, Shi S, et al. Microstructure and Mechanical Properties of In-Doped Low-Temperature SnPb Solders. Materials. 2025 Feb 18;18(4):886. doi:10.3390/ma18040886

27. Xu KK, Zhang L, Gao LL, Jiang N, Zhang L, Zhong SJ. Review of microstructure and properties of low temperature lead-free solder in electronic packaging. Sci Technol Adv Mater. 2020 Jan 31;21(1):689–711. doi:10.1080/14686996.2020.1824255

28. Gancarz T, Fima P, Pstruś J. Thermal Expansion, Electrical Resistivity, and Spreading Area of Sn-Zn-In Alloys. J Mater Eng Perform. 2014 May;23(5):1524–9. doi:10.1007/s11665-013-0825-3

29. Wang X, Cui H, Xiong Y, Li Q, Wang X, Cai S, et al. In-depth investigation of multi-element alloying on the microstructure and mechanical properties of Sn7Sb/Cu joints. J Mater Res Technol. 2025 May;36:7318–29. doi:10.1016/j.jmrt.2025.05.012

30. Gerhátová Ž, Babincová P, Drienovský M, Pašák M, Černičková I, Ďuriška L, et al. Microstructure and Corrosion Behavior of Sn–Zn Alloys. Materials. 2022 Oct 16;15(20):7210. doi:10.3390/ma15207210

31. Han S, Han SE, Lee TY, Han DG, Park YB, Yoo S. Brittle Fracture Behavior of Sn-Ag-Cu Solder Joints with Ni-Less Surface Finish via Laser-Assisted Bonding. Materials. 2024 Jul 22;17(14):3619. doi:10.3390/ma17143619

32. Wang X, Zhang L, Li M lan. Microstructure and properties of Sn-Ag and Sn-Sb lead-free solders in electronics packaging: a review. J Mater Sci Mater Electron. 2022 Feb;33(5):2259–92. doi:10.1007/s10854-021-07437-6

33. Xavier MGC, Silva BL, Spinelli JE. Advancing the Solidification of Sn–Bi Alloys for Electronic Packaging: Challenges, Progress, and Future Directions. MetalMat. 2025 Dec;2(4):e70015. doi:10.1002/metm.70015

34. El-Taher AM, Fadel MM, Eladly SA, Abd Elrahman AS, Algarni H, Ali HE, et al. Microstructural and mechanical enhancements in Sn–Ag–Cu solder alloys via nickel and bismuth additions. J Mater Sci Mater Electron. 2025 Sep;36(27):1752. doi:10.1007/s10854-025-15640-y

35. Kang Y, Choi JJ, Kim DG, Shim HW. The Effect of Bi and Zn Additives on Sn-Ag-Cu Lead-Free Solder Alloys for Ag Reduction. Metals. 2022 Jul 25;12(8):1245. doi:10.3390/met12081245

36. Xu P, Zheng X, Li L, Wang Z. Progress and Challenges in Joining for Precision Endoscope Fabrication. Sensors. 2026 May 1;26(9):2828. doi:10.3390/s26092828

37. Sayyadi R, Naffakh-Moosavy H. The Role of Intermetallic Compounds in Controlling the Microstructural, Physical and Mechanical Properties of Cu-[Sn-Ag-Cu-Bi]-Cu Solder Joints. Sci Rep. 2019 Jun 10;9(1):8389. doi:10.1038/s41598-019-44758-3

38. Wu G, Shen J, Muhammad KF, Zhou D, Wong YH, Si Z. Microstructure and mechanical properties of Cu/In–Zn–Sn–Bi/Cu joints bonded with high-entropy alloy solder at ultra-low temperature. J Mater Sci Mater Electron. 2025 Jun;36(16):926. doi:10.1007/s10854-025-14903-y

39. Ramli MII, Mohd Salleh MAA, Yasuda H, Chaiprapa J, Nogita K. The effect of Bi on the microstructure, electrical, wettability and mechanical properties of Sn-0.7Cu-0.05Ni alloys for high strength soldering. Mater Des. 2020 Jan;186:108281. doi:10.1016/j.matdes.2019.108281

40. Zhong X, Chen L, Medgyes B, Zhang Z, Gao S, Jakab L. Electrochemical migration of Sn and Sn solder alloys: a review. RSC Adv. 2017;7(45):28186–206. doi:10.1039/C7RA04368F

41. Zhou Z, Zhou K, Hou X, Luo H. Arc/Spark Optical Emission Spectrometry: Principles, Instrumentation, and Recent Applications. Appl Spectrosc Rev. 2005 May;40(2):165–85. doi:10.1081/ASR-200052001

42. Seidel P, Ebert D, Schinke R, Möckel R, Raatz S, Chao M, et al. Comparison of Elemental Analysis Techniques for the Characterization of Commercial Alloys. Metals. 2021 Apr 29;11(5):736. doi:10.3390/met11050736

43. Bengtson A. Laser Induced Breakdown Spectroscopy compared with conventional plasma optical emission techniques for the analysis of metals – A review of applications and analytical performance. Spectrochim Acta Part B At Spectrosc. 2017 Aug;134:123–32. doi:10.1016/j.sab.2017.05.006

44. Li L, Mao L, Yang J. A Review of Principles, Analytical Methods, and Applications of SEM-EDS in Cementitious Materials Characterization. Adv Mater Technol. 2025 Apr;10(7):2401175. doi:10.1002/admt.202401175

45. Li L, Yang J, Li H, Du Y. Comparative Study on Backscattered Electron Image of Cement Paste Quantified by Frequency Histogram, Overflow and Gaussian Distribution Fitting Method. J Mater Civ Eng. 2022 Jul;34(7):04022124. doi:10.1061/(ASCE)MT.1943-5533.0004272

46. Smart LE, Moore EA. Solid State Chemistry [Internet]. 0 ed. CRC Press; 2016 [cited 2026 May 26]. Available from: https://www.taylorfrancis.com/books/9781439847923 doi:10.1201/b12047

47. Martin J. Measuring resistance/impedance with the four-wire Kelvin method. Watts Curr Tech Bull. 2014;1:1–11.

48. Achternbosch M, Kupsch C, Sardemann G, Bräutigam K. Cadmium Flows Caused by the Worldwide Production of Primary Zinc Metal. J Ind Ecol. 2009 Jun;13(3):438–54. doi:10.1111/j.1530-9290.2009.00128.x

49. Fosu AY, Bartier D, Diot F, Kanari N. Insight into the Extractive Metallurgy of Tin from Cassiterite. Materials. 2024 Jul 4;17(13):3312. doi:10.3390/ma17133312

50. Huang J, Li M, Chen J, Cheng Y, Lai Z, Hu J, et al. Electronic structure and atomic migration of the fourth, fifth, and sixth period atoms in aluminum alloys: First principles calculation. Vacuum. 2023 Apr;210:111823. doi:10.1016/j.vacuum.2023.111823

51. Schwartz MO. Cadmium in Zinc Deposits: Economic Geology of a Polluting Element. Int Geol Rev. 2000 May;42(5):445–69. doi:10.1080/00206810009465091
52. Ata Esener P, Demirel B, Aksöz S. Effect of Sb and In additives on thermal and electrical properties of Sn–9Zn–4Bi alternative lead-free solder alloy. Mater Chem Phys. 2023 Feb;296:127223. doi:10.1016/j.matchemphys.2022.127223
53. Plevachuk Yu, Sklyarchuk V, Hoyer W, Kaban I. Electrical conductivity, thermoelectric power and viscosity of liquid Sn-based alloys. J Mater Sci. 2006 Jul;41(14):4632–5. doi:10.1007/s10853-006-0053-4
54. Tan XF, Hao Q, Zhou J, McDonald SD, Sweatman K, Nogita K. The Effect of Temperature on the Electrical Resistivity of Sn-Bi Alloys. J Electron Mater. 2024 Mar;53(3):1183–91. doi:10.1007/s11664-023-10849-1